magnetochemistry

MDPI

Article

$Ni_{50}Mn_{37.5}Sn_{12.5}$ Heusler Alloy: Influence of Co Addition on the Structure, Martensitic Transition, and Magnetic Properties

Ahlem Bekhouche [1,2], Safia Alleg [2], Karima Dadda [2], Benilde F. O. Costa [3], Asma Wederni [1] and Joan-Josep Suñol [1,*]

[1] Department of Physics, University of Girona, Campus Montillivi, 17071 Girona, Spain; ahlem.bekhouche@univ-annaba.dz (A.B.); asma.wederni@udg.edu (A.W.)
[2] Laboratory of Magnetism and Spectroscopy of Solids, Physics Department, Badji Mokhtar Annaba University, P.O.B. 12, Annaba 23000, Algeria; safia.alleg@univ-annaba.dz (S.A.); daddakarima21@gmail.com (K.D.)
[3] University of Coimbra, CFisUC, Physics Department, Rua Larga, 3004-516 Coimbra, Portugal; benilde@uc.pt
* Correspondence: joanjosep.sunyol@udg.edu

Abstract: The impact of Co-addition (x = 0, 2, 4, and 6 at. %) in the as-cast and annealed $Ni_{50}Mn_{37.5}Sn_{12.5}$ Heusler alloy at 900 °C for 24 h on the microstructure, magnetic properties, and the martensitic transition was studied using X-ray diffraction (XRD), scanning electron microscopy, vibrating sample magnetometry, and differential scanning calorimetry. The crystal structure of as-cast samples consists of a 14M modulated martensite structure, a face-centered (FCC) γ phase, and a face-centered tetragonal (FCT) MnNi-type phase $L1_0$. The as-cast samples show a dendritic microstructure with different contrasts and non-uniform distribution. The annealed samples exhibit dual 14M and γ phases for the Co0 and Co2, but 14M + γ + MnNi for the Co4 and Co6. The appearance of the martensitic transformation in the annealed Co0 and Co2 samples can be due to the disappearance of the dendritic microstructure. The characteristic temperatures (martensite start, *Ms*; martensite finish, *Mf*; austenite start, As; and austenite finish, *Af*) decrease with Co addition. A ferromagnetic-like order exists at a lower temperature of 1.8 K for the as-cast and annealed samples and decreases at 300 K. The annealing increases the fraction of the AFM contributions at 300 K. The exchange bias values of the Co0, An-Co2, and An-Co6 are 146.7 Oe, 24 O2, and 32.6 Oe, respectively, at 300 K.

Keywords: Ni-Mn-Sn-Co Heusler alloys; crystal structure; martensitic transformation; magnetic properties; DSC

Citation: Bekhouche, A.; Alleg, S.; Dadda, K.; Costa, B.F.O.; Wederni, A.; Suñol, J.-J. $Ni_{50}Mn_{37.5}Sn_{12.5}$ Heusler Alloy: Influence of Co Addition on the Structure, Martensitic Transition, and Magnetic Properties. *Magnetochemistry* **2024**, *10*, 59. https://doi.org/10.3390/magnetochemistry10080059

Academic Editor: Carlos J. Gómez García

Received: 12 July 2024
Revised: 7 August 2024
Accepted: 12 August 2024
Published: 15 August 2024

1. Introduction

For several years, Ni-Mn-Z (Z = Sn, In, Ga, etc.) Heusler alloys have gained much attention due to their multifunctional properties [1–4]. These significant properties mainly originated from the first-order martensitic transition (FOMT) characterized by the magneto-structural change, which is composition-dependent. The Heusler alloys may undergo a second-order magnetic transition around the martensitic Curie temperature followed by a first-order phase transition from a weak magnetic martensitic phase to a ferromagnetic austenitic phase. The indirect exchange of Mn atoms in its ferromagnetic (FM) or antiferromagnetic (AFM) state assures the magnetic tune [5]. Due to their inexpensive Ni, Mn, and Sn constituents, ternary Ni-Mn-Sn alloys have been extensively studied [6–9]. Excess in Mn atoms can occupy the regular Ni, Sn, or both Ni and Sn sites depending on the alloy composition that provides various magnetic properties [10]. Their FOMT can be modified by varying the atomic concentration ratio of the valence electrons (e/a). Therefore, substituting a fourth element in the Ni, Mn, or Sn site for the off-stoichiometric Ni-Mn-Sn alloys has been extensively studied. The structural transition temperature decreased when Co atoms substituted partially Ni atoms [11,12]. Moreover, an increase in the Curie temperature (T_C) values of both austenite and martensite phases was reported [11]. Cong et al. affirmed

the absence of the martensitic transformation (MT) for $x \geq 9$ *at*.% in $Ni_{50-x}Co_xMn_{39}Sn_{11}$ arc-melted alloys [13]. Nevertheless, by varying the Co content from 0 to 4%, they noticed a slower decrease in the martensitic transformation temperatures and a rapid diminution when x ranged from 5 to 8%. The Co addition enhanced the FM exchange coupling in $Ni_{43}Mn_{46-x}Co_xSn_{11}$ alloys [14] and raised the magnetic entropy change (ΔS), which reached 33 J/kg·K under an external magnetic field up to 5 T. When the Co substituted the Mn atom, this improved the magnetization and enhanced the Curie temperature [15]. Similarly, the martensitic transformation temperature increased, as depicted by Liu et al. [16]. However, it did not increase monotonously for the arc-melted $Ni_{50}Mn_{36-x}Co_xSn_{14}$ alloy [17]. Wang et al. noticed an increase of about 25 K in the martensitic transformation temperature by adding 2 at. %Co to the $(Ni_{49}Mn_{39}Sn_{12})_{100-x}Co_x$ arc-melted alloy [18].

Adding a fourth element like Co, Fe, and Cu in the Heusler alloys improves their ductility by forming the disordered face-centered cubic (FCC) γ phase. This ductile phase does not participate in the martensitic phase transition, and its presence compromises the shape memory effect by hindering the activities of the martensite variants and decreasing the shape memory recovery of strain as its amount increases. Furthermore, the morphology of the γ phase is significant in toughening the alloys. Due to the high potential of Co-doped Ni-Mn-Sn alloys for engineering applications, it is necessary to understand the formation mechanism of the γ phase and provide more information on the crystal structure with Co-doping. Furthermore, the Ni-Mn-Sn Heusler alloys have shown substantial modifications in their microstructural and magnetic properties upon solidification using different molds. Co-doping plays a crucial role in modifying the magnetic characteristics of Ni-Mn-Sn Heusler alloys, such as saturation magnetization, magnetic entropy change, and magnetic behavior across structural transformations.

This work aims to contribute to a deeper understanding of the microstructural changes and magnetic characteristics of Co-doped Ni-Mn-Sn Heusler alloys. The effect of Co-substitution for Ni, Mn, or Sn sites in the $(Ni_{50}Mn_{37.5}Sn_{12.5})_{100-x}Co_x$ (x = 0, 2, 4, and 6 at. %) quaternary alloys on the structure, microstructure, thermal stability, and magnetic properties is studied using X-ray diffraction (XRD), scanning electron microscopy (SEM) coupled with energy dispersive X-ray spectroscopy (EDS), differential scanning calorimetry (DSC), and vibrating sample magnetometry (VSM).

2. Materials and Methods

Polycrystalline $(Ni_{50}Mn_{37.5}Sn_{12.5})_{100-x}Co_x$ (x = 0, 2, 4, and 6 at. %) Heusler alloys, denoted as Co0 (x = 0), Co2 (x = 2), Co4 (x = 4), and Co6 (x = 6), were produced from pure (99.98%) Ni, Mn, Sn, and Co elements (Sigma-Aldrich, Saint Louis, MO, USA) using arc melting in a MAM-1 (Edmund Bühler GmbH, Bodelshausen, Germany) arc melter, under argon atmosphere in a water-cooled copper crucible. The samples were re-melted several times to ensure a good homogeneity of the alloys. Each ingot, of approximately 15 mm in diameter, was sectioned from the center region into two pieces. One piece was wrapped in a tantalum foil, annealed in a quartz capsule at 900 °C for 24 h, and then quenched in iced water to avoid the formation of intermediate phases during the cooling process. The samples are labeled as An-Co0, An-Co2, An-Co4, and An-Co6 for simplicity.

The effect of the Co-substitution on the crystal structure was examined by a powder D8 Advance diffractometer (Brucker, Billerica, MA, USA) X-ray diffractometer (XRD) in a θ–2θ Bragg Brentano geometry using an applied voltage of 40 kV, a current of 40 mA, and a Cu-Kα radiation (λ_{Cu} = 1.54060 Å). The Rietveld refinement using the MAUD program [19] was employed to determine the crystal structure, phases' weight fraction, average crystallite size, <*L*>, and lattice parameters (*a*, *b*, *c*). A scanning electron microscope (SEM) Zeiss DSM-960A (Siemens/Brucker, Billerica, MA, USA) equipped with energy dispersive X-ray spectrometry (EDS) was utilized to determine the alloys' microstructure and elemental composition.

Thermal characterization was performed in a differential scanning calorimeter DSC131 EVO (Setaram , Caluire-et-Cuire, France) in the 25–150 °C temperature range at a heat-

ing/cooling rate of 5 °C/min for four cycles. A vibration sample magnetometer (VSM) with a cryogen-free Dynacool PPMS was used at a vibration frequency of 40 Hz and 2 mm amplitude in the coils' central area. Small bulk samples were put in a rod-shaped Perspex sample holder. Hysteresis loops (M vs. μ_0H) at 300 K and 1.8 K were measured under an external magnetic field up to 9 T; zero-field-cooled (ZFC) and field-cooled (FC) curves of the as-cast and annealed alloys were measured in a magnetic field of 0.5 T.

3. Results and Discussion

3.1. Crystal Structure

The XRD patterns of the as-cast $(Ni_{50}Mn_{37.5}Sn_{12.5})_{100-x}Co_x$ (x = 0, 2, 4 and 6 at. %) alloys are shown in Figure 1. The effect of the Co-substitution is correlated to the shift in the diffraction peaks towards higher 2-theta angles as the Co content increases. The slight shift in the peak position can be attributed to the lattice strains and the variation in the lattice parameters of the martensite structure due to the substitution of Co for Ni, Mn, or Sn since the atomic size of Co (r_{Co} = 0.135 nm) is close to that of Ni (r_{Ni} = 0.135 nm) but smaller than those of Mn (r_{Mn} = 0.140 nm) and Sn (r_{Sn} = 0.150 nm). Furthermore, the principal diffraction peak intensity increases as the Co content augments, excluding the Co2 sample. Such a rise can be due to the increase in the crystallite size and/or the variation in the phase's weight fractions.

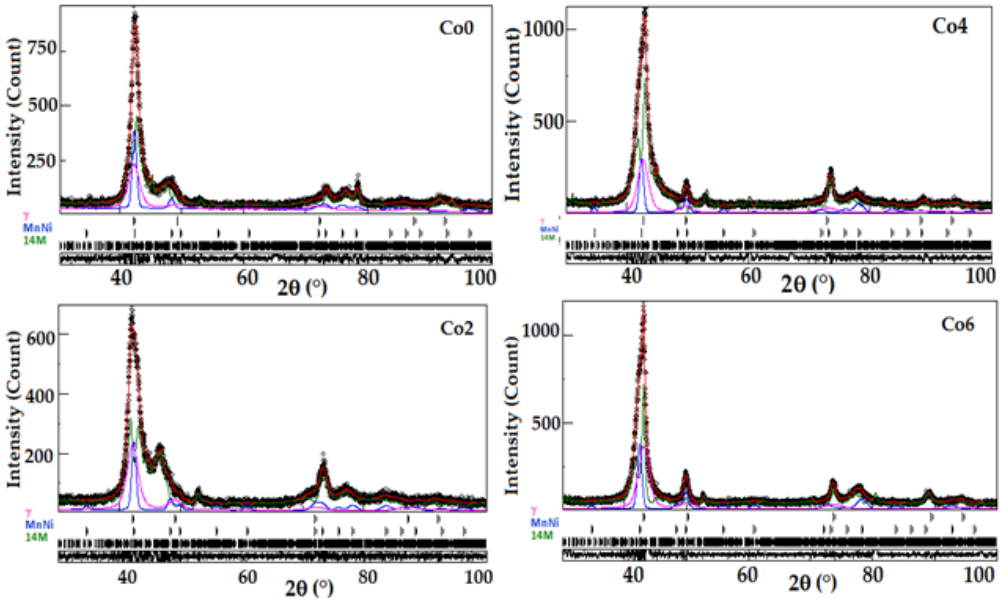

Figure 1. Rietveld refinement of the XRD patterns of Co0, Co2, Co4, and Co6 as-cast alloys.

The Rietveld refinement reveals the presence of three phases, namely the monoclinic 14M martensite structure (P21/m space group), the FCC γ phase (space group Fm-3m), and the face-centered tetragonal (FCT) MnNi-type phase $L1_0$ (P4/mmm space group). The formation of three phases can be due to numerous factors, such as the alloy composition, preparation conditions, phase transformation thermodynamics, etc. This result agrees well with previous studies that reported the presence of several phases in the NiMnSn alloys depending on the alloy composition and preparation conditions [13–18]. The crystallite size of the 14M, γ, and MnNi-type $L1_0$ phases are in the range of (20–30) nm, (9–10) nm, and 87 nm, respectively (Table 1). The weight fraction of the γ phase increases slightly from 21% for the Co0 to 30, ~31, and ~34% for the Co2, Co4, and Co6, respectively. The weight fraction of the FCT MnNi exhibits an opposite trend to that of the 14M Heusler phase (Figure 2). Such a variation might be due to the movement of Ni, Mn, Co, and Sn atoms.

Table 1. Lattice parameters (*a*, *b*, and *c*), average crystallite size (<*L*>), and reliability factors (*Gof*, and *Rwp*) of as-cast samples.

Sample	Phase	a (Å) ± 10^{-4}	b (Å) ± 10^{-4}	c (Å) ± 10^{-4}	β (°)	<L> (nm) ± 2	Rel. Factors
Co0	14M	4.3839	5.6274	29.4170	92.566	29	Gof = 1.13
	MnNi	2.5848	---	3.7598	90.00	87	R_{wp} = 12.11%
	γ	3.7118	---	---	90.00	09	
Co2	14M	4.3740	5.6278	29.3975	92.679	20	Gof = 1.09
	MnNi	2.5851	---	3.7634	90.00	87	R_{wp} = 12.97%
	γ	3.7054	---	---	90.00	10	
Co4	14M	4.3455	5.6279	29.3552	92.598	22	Gof = 1.28
	MnNi	2.5835	---	3.7594	90.00	87	R_{wp} = 13.29%
	γ	3.6652	---	---	90.00	9.5	
Co6	14M	4.3037	5.6383	29.3480	92.629	30	Gof = 1.17
	MnNi	2.581	---	3.7604	90.00	87	R_{wp} = 13.08%
	γ	3.6424	---	---	90.00	10	

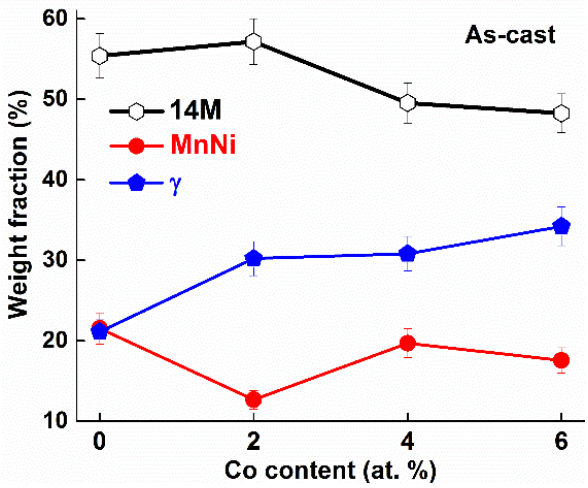

Figure 2. Evolution of the phase's weight fractions in the as-cast state vs. Co content.

The lattice parameter *a* of the γ phase decreases, while that of the MnNi phase remains unchanged, but *c* shows a slight increase for the Co2 and a linear decrease as the Co content increases. For the 14M phase, the lattice parameters *a* and *c* decrease as the Co content increases, while *b* remains nearly constant up to 4%Co and then increases slightly. The decrease in the lattice parameters leads to unit cell volume contraction. Furthermore, the variation in the lattice parameters can be related to the variation in the phases' composition due to the diffusion process and the substitution of Co atoms with a smaller atomic radius for Mn and/or Sn. A higher lattice parameter of 3.903 Å was obtained for the γ phase in the $Ni_{38}Co_{12}Mn_{41}Sn_9$ as-cast alloy [20], where the Co content improved and the Sn content lowered to 2.31%. The lattice parameter value can be related to the crystal distortion (contraction/expansion) through the diffusion of atoms with greater/smaller atomic radii. Furthermore, the formation of the γ phase leads to a change in the composition of the matrix.

Figure 3 displays the Rietveld refinement of the XRD patterns of the annealed samples. The effect of annealing is evidenced by the increase in the intensity of some diffraction peaks and the change in their shape, principally for the An-Co0, An-Co4, and An-Co6 samples. A crystallographic texture with a grain-oriented microstructure of the 14M martensite along the [0014] and [1020] directions for the An-Co0 and [1114] and [1020] directions for the An-Co4 is depicted. This behavior arises from the rapid cooling of the annealed samples.

The crystallite size of the 14M structure and γ phase decreases with increasing the Co content up to 4 at. % and then increases for the An-Co6 sample (Table 2). The crystallite size refinement might be related to the structural disorder through the Co diffusion into the

Heusler matrix. The weight fraction of the γ phase increases linearly from approximately 24.5% for the An-Co0 to 46.4% for the An-Co6. Simultaneously, the weight fraction of the 14M Heusler phase (Figure 4) decreases as the Co content increases while that of the MnNi increases.

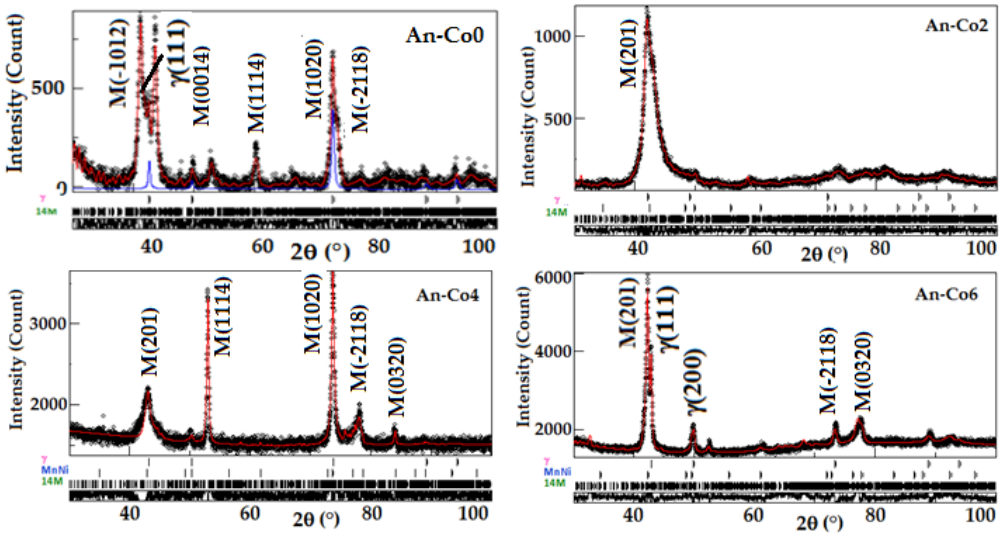

Figure 3. Rietveld refinements of the XRD patterns of An-Co0, An-Co2, An-Co4, and An-Co6 alloys.

Table 2. Lattice parameters (*a*, *b*, and *c*), average crystallite size (<*L*>), and reliability factors (*Gof*, and *Rwp*) of annealed samples.

Sample	Phase	*a* (nm) $\pm 10^{-4}$	*b* (nm) $\pm 10^{-4}$	*c* (nm) $\pm 10^{-4}$	β (°)	<*L*> (nm) ±2	Rel. Factors
An-Co0	14M	4.3810	5.4124	29.4011	92.770	92	Gof = 1.13
	γ	3.6674	---	---	90.00	45	Rwp = 3.14%
An-Co2	14M	4.3803	5.6271	29.4152	92.610	64	Gof = 1.09
	γ	3.7082	---	---	90.00	10	Rwp = 8.79%
An-Co4	14M	4.3100	5.6418	29.352	92.563	48	Gof = 1.29
	MnNi	2.5239	---	3.7416	90.00	95.4	R_{wp} = 3.22%
	γ	3.6580	---	---	90.00	11.0	
An-Co6	14M	4.3046	5.6902	29.189	92.351	60	Gof = 1.17
	MnNi	2.6018	---	3.7344	90.00	50	R_{wp} = 13.08%
	γ	3.6497	---	---	90.00	99	

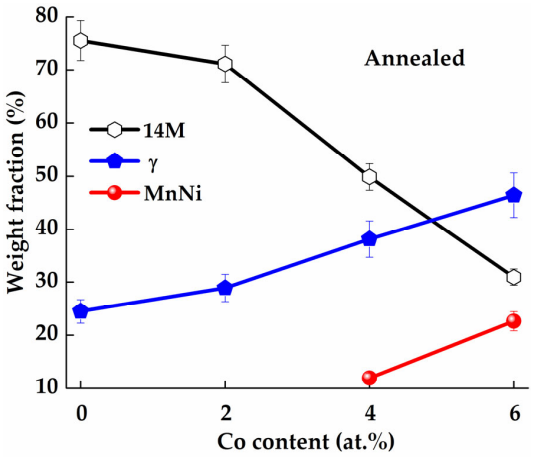

Figure 4. Evolution of the phase's weight fractions in the annealed alloys vs. Co content.

3.2. Morphology and Elemental Analysis

The back-scattered (BSE) SEM morphologies in the as-cast state (Figure 5) revealed the effect of Co-substitution in the Ni-Mn-Sn Heusler alloy. The produced alloys exhibit a dual microstructure of coarse dendritic phase and lamellar hypoeutectic microstructure with a change in the contrast from gray (matrix) and dark (γ phase) for the Co0 and Co2 alloys to light (matrix) and dark (γ phase) for the Co4 and Co6 alloys. The variation in the contrast of the SEM images suggests compositional differences between the different phases and the existence of at least two phases depending on the alloy composition. The variation in the contrast can be related to the alteration in the phases' compositions as the cobalt concentration augments, in addition to the enlargement of the lamellar eutectic microstructure (dark contrast). The formation of dendritic multiphasic microstructure can be related to the occurrence of the eutectic reaction during the solidification process [21,22]. The non-equilibrium solidification of the eutectic phases is due to the fast cooling rate of the arc melting technique. The presence of black particles with different shapes and a non-uniform distribution should also be noted. The EDS analysis of the Co-free alloy reveals that the elemental composition is close for both contrasts with 44.03Mn-48.6 Ni-7.37Sn (at. %) for the gray contrast and 44.66Mn-48.04 Ni-7.29Sn (at. %) for the dark contrast.

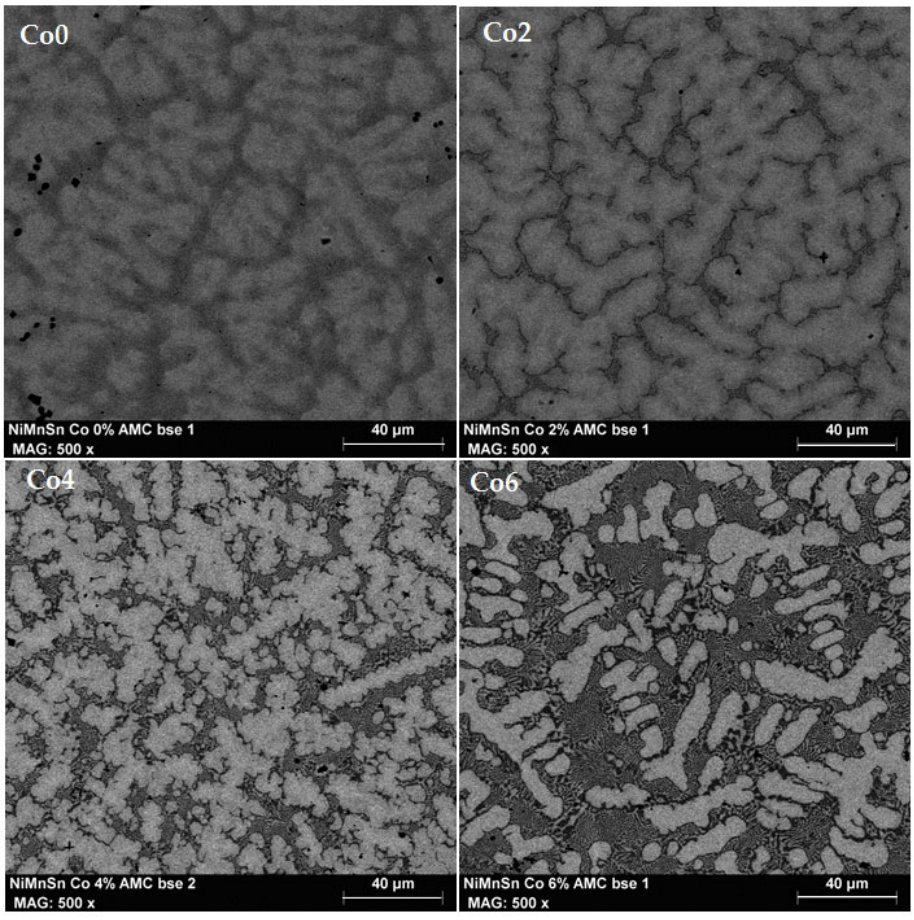

Figure 5. Back-scattered SEM images of the as-cast $Ni_{50}Mn_{37.5}Sn_{12.5}$ alloy as a function of the cobalt content (Co0, Co2, Co4, and Co6).

The elemental analysis of the as-cast Co6 alloy (Figure 6) reveals that the composition of the Heusler phase is nearly constant with average Mn, Ni, and Sn contents in the Heusler phase of approximately 46.68 at. %, 41.79 at. %, and 11.53 at. %, respectively. A closer examination shows the presence of at least three phases in addition to the heterogeneity of

the as-cast alloys with strong segregation, a typical microstructure of the as-cast alloys. The Heusler phase is a Ni-Mn-Sn phase, while the γ phase is principally a Ni-Mn-Co with a small Sn content. This observation agrees well with those reported in similar systems [23,24]. The black particles with irregular shapes and sizes (Figure 6c) can be related to highly Mn-rich Mn-Ni precipitates. According to the elemental mapping images for Ni, Mn, Sn, and Co (Figure 7), the γ phase is Co-rich and poorer in Sn compared to the Heusler phase, but the fluctuations in Ni and Mn concentrations are relatively slight between the Heusler and γ phase. The variation in the Heusler phase composition affects the e/a ratio and the martensitic transformation. It has been reported that a decrease in the e/a ratio leads to a drop in the martensitic transformation temperature [25].

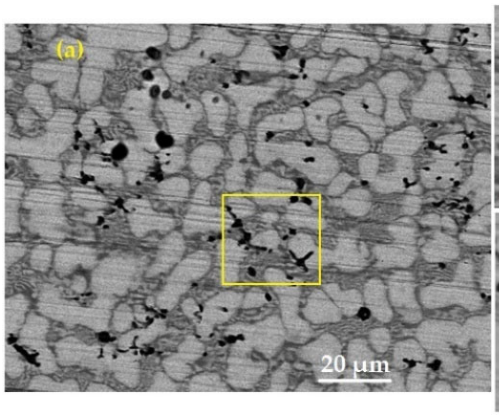

Spot	Mn	Ni	Sn	Co
1	46.39	41.81	11.81	---
2	46.98	41.77	11.25	---
3	42.46	48.85	2.12	6.57
4	40.60	50.58	5.36	3.46
5	41.08	49.61	4.72	4.59

Spot	Mn	Ni	Sn	Co
1	88.72	8.79	0.16	---
2	90.88	7.02	0.14	---
3	87.19	10.54	1.56	0.71

Figure 6. Back-scattered SEM image of as-cast Co6 alloy (**a**); (**b**,**c**) enlarged from (**a**). The elemental composition from spots in (**b**,**c**) is given in Table (**right**).

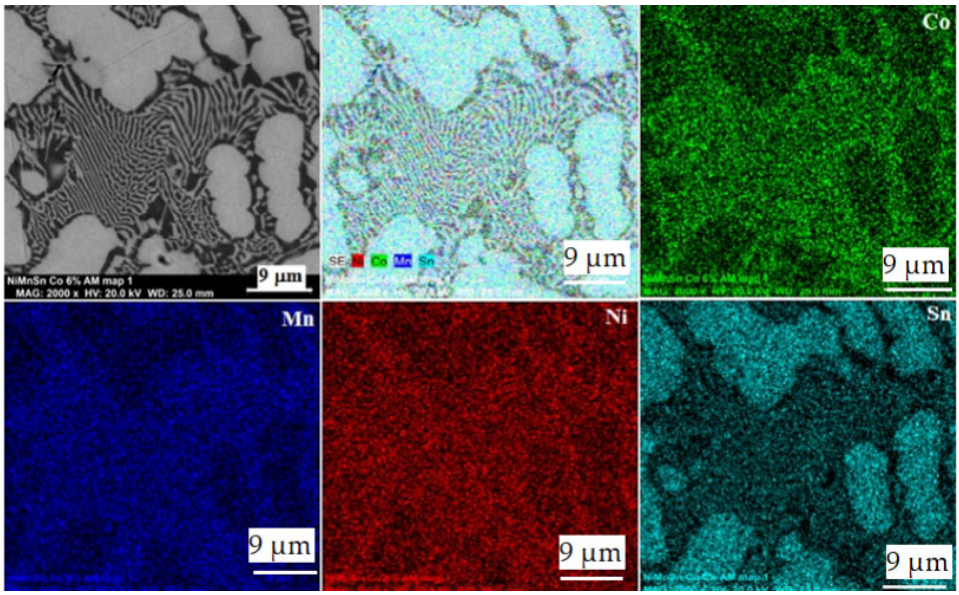

Figure 7. Elemental mapping for Ni, Mn, Co, and Sn in the as-cast Co6 alloy.

Figure 8 depicts the back-scattered SEM micrographs of annealed An-Co0, An-Co2, An-Co4, and An-Co6 alloys. The Co-free alloy (An-Co0) undergoes a homogeneous microstructure and the transformation of the inter-dendritic region in the Heusler phase through the diffusion process. Furthermore, the black precipitates are still observed even after annealing for 24 h. The An-Co2 alloy shows the transformation of the dendritic microstructure and the presence of mainly two phases: the Heusler phase (matrix) and the γ phase. However, the dendritic microstructure remains for both the An-Co4 and An-Co6

alloys. The elemental mapping images for Ni, Mn, Sn, and Co (Figure 9) show that the Heusler phase is Sn-rich and poorer in Co compared to the γ phase, while the Ni and Mn concentrations fluctuate slightly in the Heusler phase.

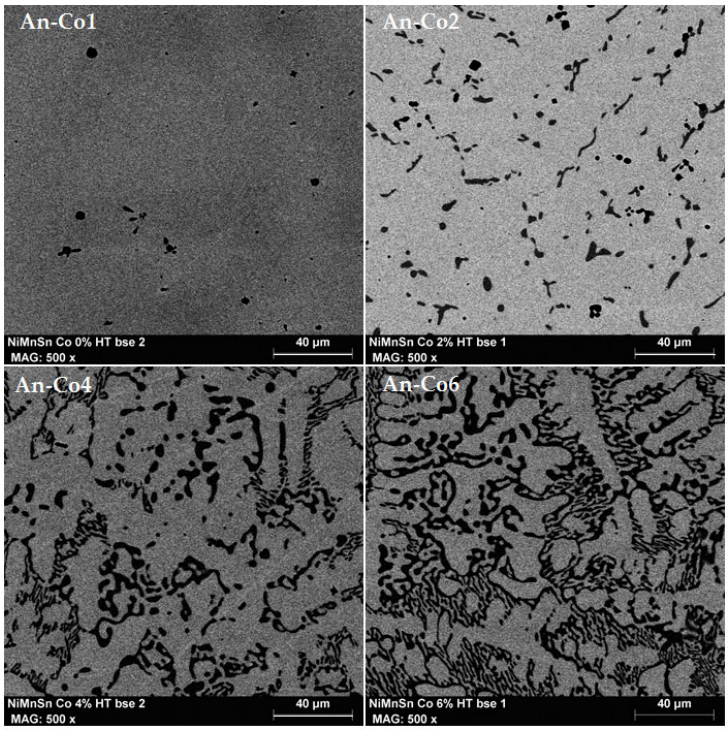

Figure 8. Back-scattered SEM images of the annealed $Ni_{50}Mn_{37.5}Sn_{12.5}$ alloy as a function of the cobalt content (An-Co0, An-Co2, An-Co4, and An-Co6).

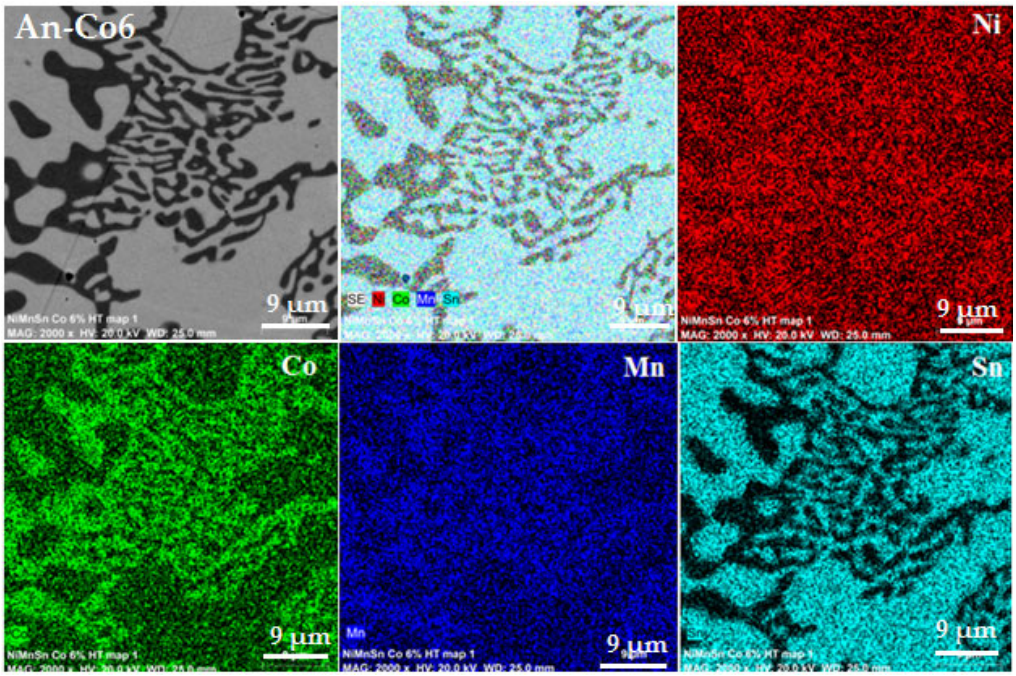

Figure 9. Elemental mapping for Ni, Mn, Co, and Sn in the An-Co6 alloy.

3.3. Thermal Analysis

The DSC scans of the annealed An-Co0, An-Co2, An-Co4, and An-Co6 samples at 900 °C for 24 h are displayed in Figure 10 within the temperature range 30–150 °C. Upon heating and cooling at 5 °C/min for four cycles, the Co0 and Co2 samples exhibit an endothermic peak on heating and an exothermic peak upon cooling related to forward and reverse martensite transitions, respectively. The appearance of the martensite transformation in the An-Co0 and An-Co2 samples can be due to the suppression of the dendritic microstructure, as observed in the SEM images in Figure 8. However, the Co4 and Co6 samples show only broad endothermic and exothermic peaks on heating and cooling, leading to the inaccurate determination of the martensitic transformation temperatures. The broad thermal event might be related to the heterogeneity of the samples and compositional disparity, as revealed in the EDS analysis. Furthermore, the absence of the martensitic transformation in the as-cast alloys can be related to the dendritic microstructure since the martensite transition is highly sensitive to the alloy composition, and the non-uniform compositional variations affect the martensitic transformation for all the as-cast samples. However, after annealing at 900 °C for 24 h, the martensitic transition occurs once the chemical and/or structural homogenization is achieved for the An-Co0 and An-Co2 samples, but significant fluctuation compositions remain for the An-Co4 and An-Co6 samples as revealed by the SEM images. Much longer annealing times are needed for compositional homogeneity as the Co content increases. Similar comportment was reported for the Ni-Mn-Sn Heusler alloys [26]. Table 3 lists the martensitic transformation temperatures such as the martensite start (M_{st}), martensite finish (M_f), austenite start (A_{st}), austenite finish (A_f) as well as the thermodynamic parameters on cooling (c) and heating (h), including the enthalpy (ΔH) and the entropy (ΔS) of transformation. It should be noted that all the parameters decrease for the An-Co2 sample compared to the An-Co0. It has been reported that during both austenite and martensite transformation, the transformation energies were low and the peaks were broad in the Ni 50 Mn 36 Sn 12 Co 2 (at. %) produced by arc melting and subsequent aging at 900 °C [27].

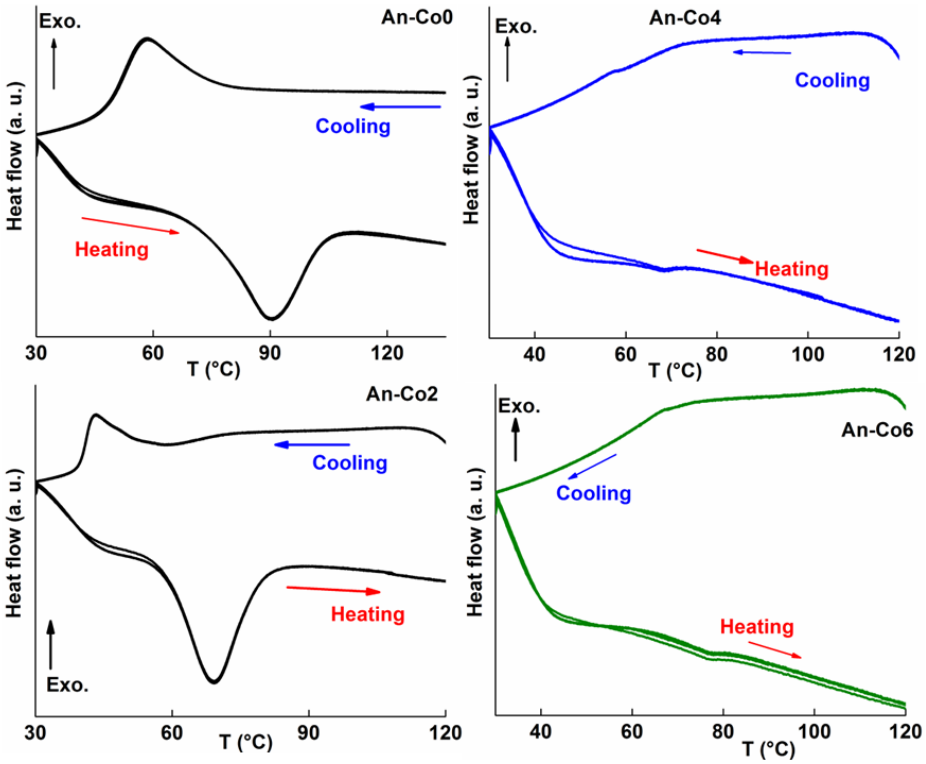

Figure 10. DSC scans on heating/cooling of the of the An-Co0, An-Co2, An-Co4, and An-Co6 alloys.

Table 3. Martensite start/finish (M_{st}/ M_f), and austenite start/finish (A_s/A_f), temperatures (ΔT), ΔH, and ΔS on heating (h) and cooling (c) of the An-Co0 and An-Co2 samples.

Sample	A_s (°C)	A_f (°C)	M_{st} (°C)	M_f (°C)	ΔT (°C)	ΔH (J/g)	ΔS (J/gK)
An-Co0	71	105	82	54	78	79.76 (h) 85.55 (c)	1.0225 (h) 1.0967 (c)
An-Co2	57	80	46	40	55.75	44.78 (h) 14.24 (c)	0.8032 (h) 0.2554 (c)

The calculated equilibrium transformation temperature using $T_0 = \frac{M_{st}+M_f+A_s+A_f}{4}$ decreases from 78 °C for An-Co0 to 55.75 °C for the An-Co2 sample due to the reduction in the e/a ratio of the matrix. Furthermore, both the enthalpy change (ΔH) and entropy change (ΔS) of the transformation of the An-Co2 decrease compared to the An-Co0 sample. It is evident that the Co addition has altered the matrix composition and produced various transforming alloys and different entropy changes in these alloys. Furthermore, the thermal hysteresis temperature $\Delta T = \frac{M_{st}+A_f-M_f-A_s}{4}$ drops from 62 °C for the An-Co0 to 29 °C for An-Co2 samples (Table 3). The enthalpy of the martensite transformation during cooling in the An-Co2 is three times smaller than that during heating. This difference might be related to the increased amount of the γ phase that did not participate in the martensitic transformation and/or to the variation in the matrix composition that alters the transformation.

3.4. Magnetic Properties

The temperature dependence of magnetization ($M-T$) curves at the field-cooled (FC) and zero-field-cooled (ZFC) modes are shown in Figures 11 and 12 for the as-cast and annealed samples, respectively. During ZFC recording, the sample was initially cooled to the minimal temperature that could be achieved at zero magnetic fields, and the measurements were registered during heating runs under an applied magnetic field of 0.5 T. The ZFC curves show different behaviors as a function of the Co content. The magnetization increases progressively for the Co0 and Co4 as the temperature is raised to 300 K, increases to 50 K, and remains nearly constant for the Co2. For the Co6 sample, the magnetization reaches a maximum value of about 60 K, which defines the spin freezing temperature (T_B). After T_B, the magnetization decreases. Furthermore, the split of the ZFC and FC curves that define the irreversibility temperature (T_{irr}) results from the coexistence of antiferromagnetic (AFM) and ferromagnetic (FM) phases. This behavior is due to the presence of Mn in the NiMnSn crystalline structure [28].

In the Ni-Mn-based Heusler alloys, the magnetization is attributed principally to Mn atoms where the Mn-Mn exchange is FM in the stoichiometric 2:1:1 alloy obeying the Ruderman–Kittel–Kasuya–Yosida (RKKY) coupling granted by the conducting electrons. However, in the off-stoichiometric structure, the exchange between the excess Mn content occupying the Z site and Mn in its regular site is AFM as the Mn-Mn distance is shortened. The presence of both FM and AFM ordering competitors generates a low magnetic state of the martensite phase [29] and evidences the irreversibility in ZFC-FC curves [30,31]. One notes that the magnetization shows a step-like nature within ~50 K and 150 K in ZFC curves, which can be related to the blocking temperature of the martensitic phase (T_B) promoting the exchange bias effect (E_B). Below 50 K, the ZFC plot decreases due to the dominated AFM state and AFM zones that pin the FM spin structure. Remarkably, the split between ZFC and FC curves converge at T_{split} at around 300 K. The FC measurements are higher than those of ZFC ones and tend to increase by lowering the temperature due to the coexistence of FM/AFM coupling at the martensitic phase [32]. The Zeeman energy provided by the external field dismisses this FM/AFM coupling and then bifurcates the ZFC and FC curves.

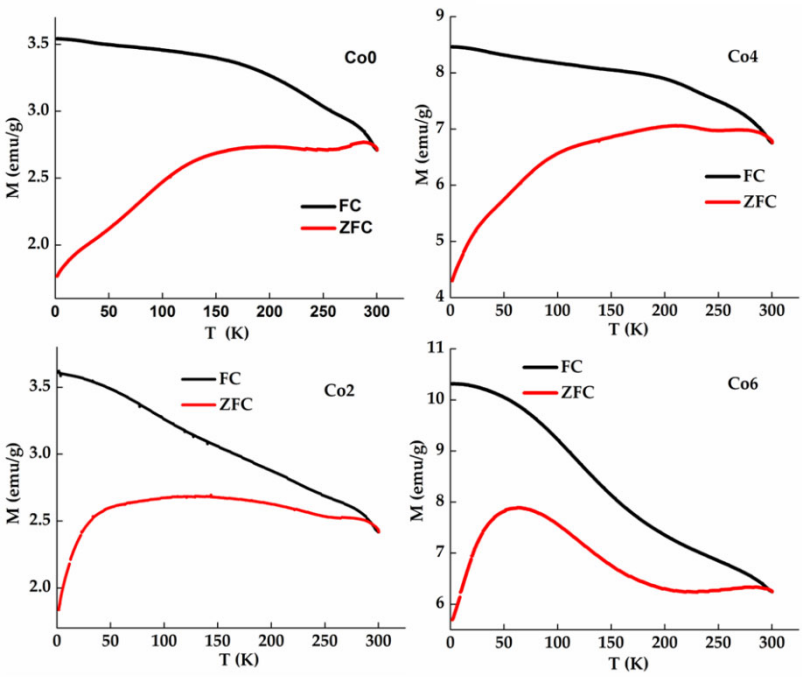

Figure 11. FC and ZFC magnetization curves for as-cast Co0, Co2, Co4, and Co6 samples.

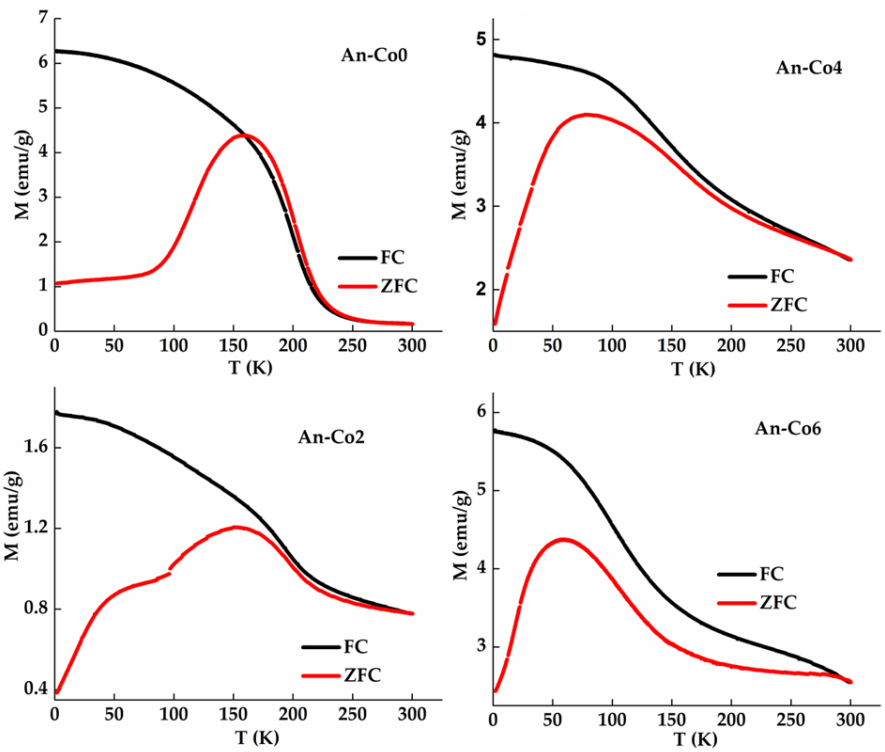

Figure 12. FC and ZFC magnetization curves for annealed An-Co0, An-Co2, An-Co4, and An-Co6 samples.

Figure 13 shows the hysteresis loops taken at 1.8 K and 300 K for the as-cast and annealed alloys. At 1.8 K, all samples reveal a ferromagnetic-like behavior that does not saturate even under a strong magnetic field. For the as-cast alloys, the magnetization increases as the Co content increases, except for the Co2, which diminishes slightly. The same behavior is observed for the annealed sample, where the magnetization decreases for the An-Co2 and then increases for the An-Co6, while that of the An-Co4 is nearly similar to the An-Co0. The magnetization of all the samples decreased when performing

the measurements from 1.8 K to 300 K. The variation in the magnetization might be related to the crystal structure and the change in the lattice parameters of the 14M and/or MnNi structures.

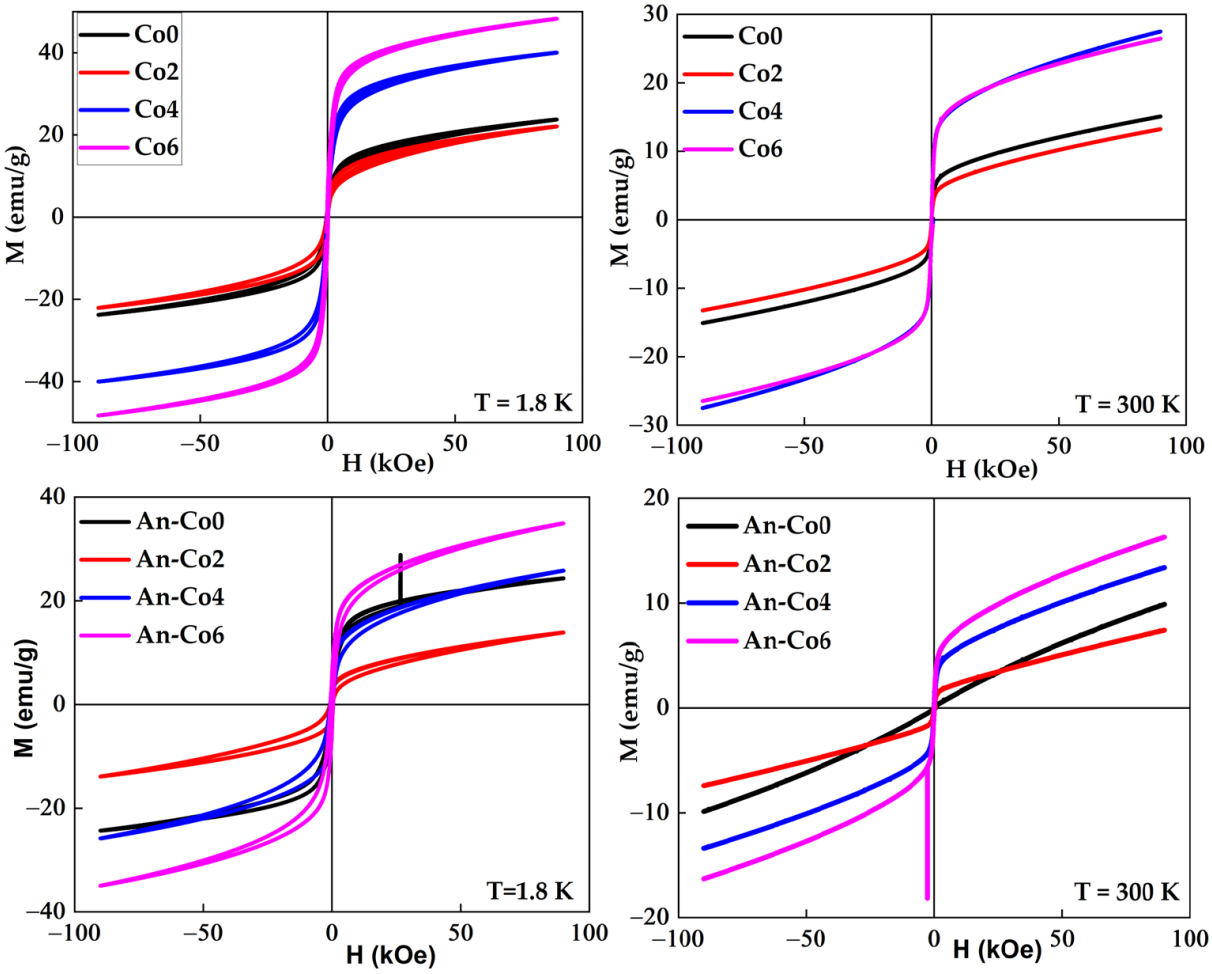

Figure 13. As indicated, hysteresis cycles were recorded at 1.8 and 300 K for the as-cast (**top**) and annealed (**down**) samples.

The curve obtained at RT for the An-Co0 sample shows negligible FM behavior but exhibits a slight exchange bias (EB). The EB is observed for the as-cast Co2 and Co6 samples, measured at RT. These samples' exchange bias field (HE) is 146.7 Oe, 24.0 Oe, and 32.6 Oe for An-Co0, Co2, and Co6, respectively. These values follow those for the same parameters in similar Heusler systems [33,34].

Magnetization hysteresis loops at room temperature do not saturate, suggesting the existence of para- or antiferromagnetic contribution to the M-H curves. This behavior is well known and the paramagnetic/AFM contribution is usually subtracted to theoretically determine the intrinsic FM parameters, such as the ferromagnetic saturation magnetization (M_s), the remnant magnetization (M_r), and the intrinsic coercivity (H_{ci}) using the following fitting function [35]:

$$M(H) = 2\frac{M_s}{\pi} tan^{-1}\left(\left(\frac{H \pm H_{ci}}{H_{ci}}\right) tan\left(\frac{\pi \times M_r}{2 \times M_s}\right)\right) + \chi H \quad (1)$$

The first term represents the ferromagnetic (FM) hysteresis curve, and the second term is a linear contribution related to a possible antiferromagnetic contribution (AFM) due to the presence of both the FCC γ- and FCT MnNi-type phases. We evaluated the percentage of FM and AFM contributions in each sample, using the M(H) curves at RT, except for

Co-0%, for which remnant magnetization was negligible so that the fitting to the used Equation (1) was not possible.

The results of the fitting procedure are shown in Figure 14, and the obtained percentages of FM and AFM contributions are depicted in Figure 15 for the as-cast and annealed samples. Both the FM and AFM contributions exhibit similar tendencies. The FM contribution increases slightly for An-Co4, and then decreases An-Co6. Furthermore, the homogenization at 900 °C increases the AFM percentages for all the samples (as well as for the sample with Co0, as seen in M(H) curves). The increase in the AFM percentage might be related to the atomic ordering enhancement and the strengthening of Mn-Mn interactions favoring antiferromagnetic alignment and reducing the frustration in magnetic interactions. The increase in the AFM contribution agrees well with the XRD results where the weight fraction of the 14M structure decreases while those of the Mn-rich MnNi and γ phases increase. Furthermore, the EDS analysis reveals the presence of Mn-rich zones.

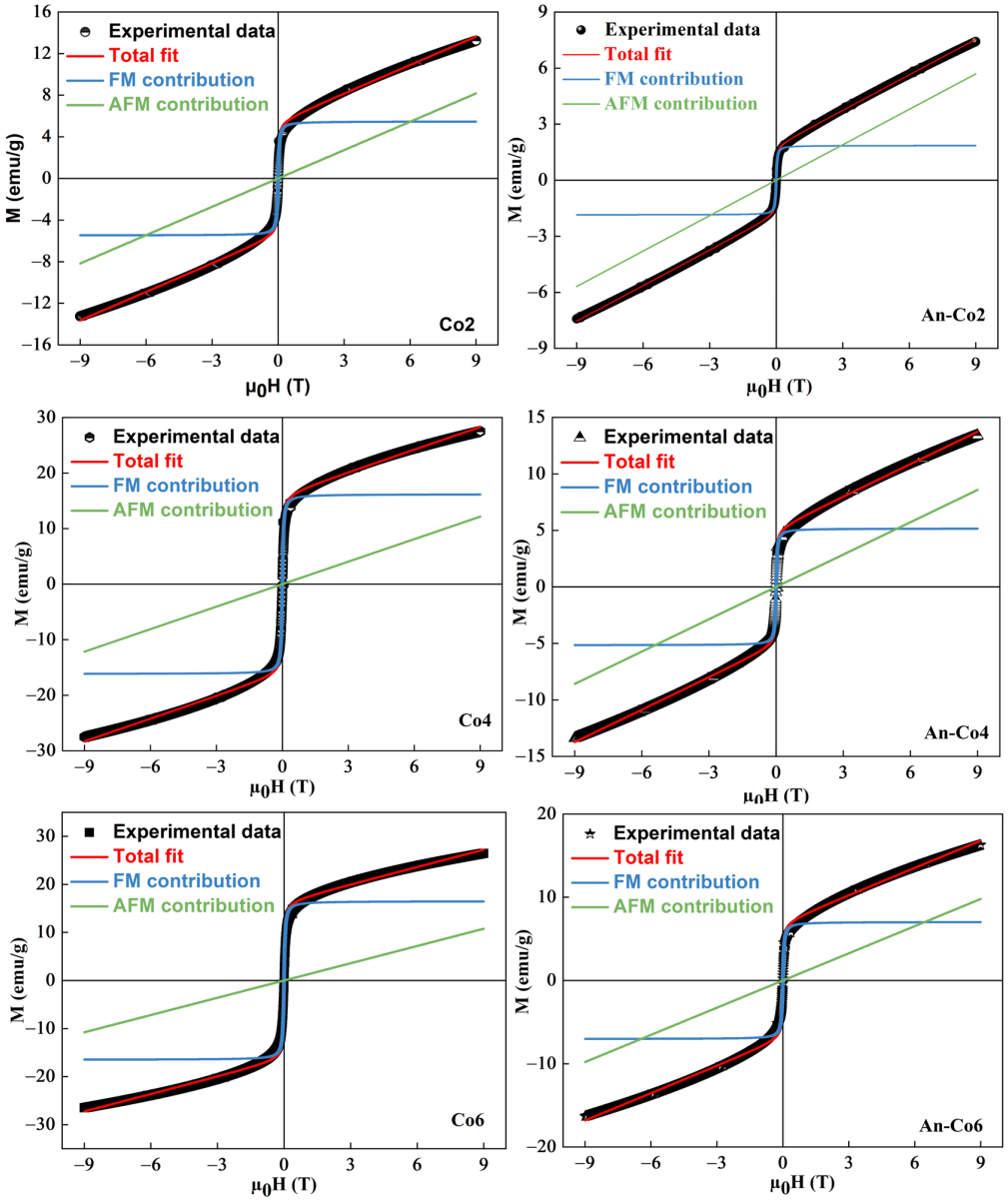

Figure 14. Fitting of the data shown in Figure 12, measured at RT, with FM and AFM contributions, for the as-cast and annealed samples at 900 °C for 24 h, as indicated.

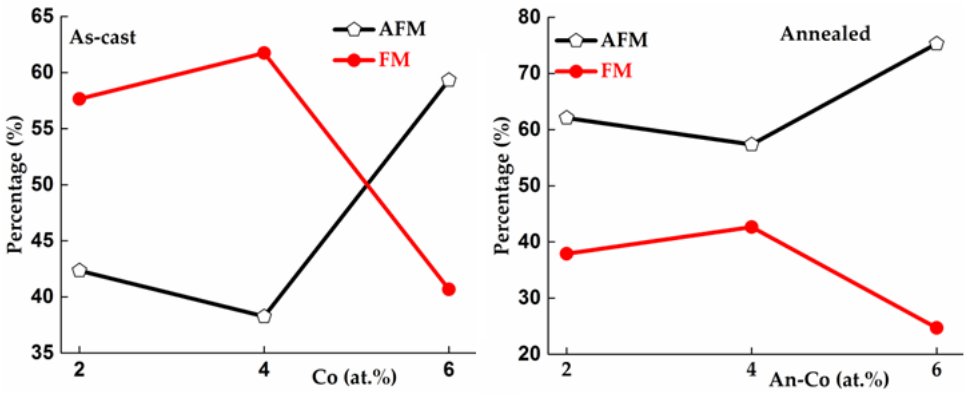

Figure 15. FM and AFM percentages at RT, obtained from the fitting procedure shown in Figure 13.

4. Conclusions

The effect of Co doping on the microstructure, martensitic transition, and magnetic properties of the $Ni_{50}Mn_{37.5}Sn_{12.5}$ Heusler alloy prepared by arc melting and subsequent annealing at 900 °C for 24 h has been investigated. The absence of the martensitic phase transition in the as-cast samples can be due to the dendritic microstructure and variation in the Heusler phase composition. The appearance of the martensite transformation in the An-Co0 and An-Co2 samples can be related to the disappearance of the dendritic microstructure, as revealed by the SEM images. The Co addition decreases the characteristic temperatures (A_s, A_f, M_s, and M_f).

The XRD results confirm the presence of the monoclinic 14M, the FCC γ phase, and the FCT MnNi-type structure for as-cast, An-Co4, and An-Co6 samples. The An-Co0 and An-Co2 samples exhibit dual 14M and γ phases. The crystallite sizes of all the phases are on the nanometer scale.

A ferromagnetic-like order exists at a lower temperature of 1.8 K for the as-cast and annealed alloys. The percentage of FM and AFM contributions were evaluated using the M(H) curves at RT except for Co0. The annealing increases the AFM percentages for all the samples. The EB values of the Co0, An-Co2, and An-Co6 are 146.7 Oe, 24 Oe, and 32.6 Oe, respectively, at 300 K.

Author Contributions: Conceptualization, S.A.; methodology, S.A.; software, S.A., K.D. and A.B.; validation, S.A., A.W. and J.-J.S.; formal analyses, S.A., K.D., A.B., A.W. and B.F.O.C.; investigation, K.D. and B.F.O.C.; resources, S.A. and J.-J.S.; data curation, S.A.; writing—original draft preparation, S.A.; writing—review and editing, S.A., K.D. and B.F.O.C.; visualization, S.A.; supervision, S.A.; project administration, S.A. and J.-J.S. All authors have read and agreed to the published version of the manuscript.

Funding: Financial support from The Directorate-General for Scientific Research and Technological Development (DGRSDT), MESRS Algeria, and Erasmus+ KA107 are acknowledged. This study was funded by the University of Girona PONT2020-01 and MINECO Spain MAT2016-75967-P projects.

Data Availability Statement: Data are available upon request to the authors.

Acknowledgments: The authors thank Foued KHAMMACI from the LM2S Laboratory for XRD and DSC measurements. Access to TAIL-UC facility funded under QREN-Mais Centro Project No. ICT_2009_02_012_1890 is gratefully acknowledged.

Conflicts of Interest: The authors declare no conflicts of interest.

References

1. Umetsu, R.Y.; Xiao, X.; Kainuma, R. NiMn-based metamagnetic shape memory alloys. *Scripta Mater.* **2016**, *116*, 1–6. [CrossRef]
2. Bachagha, T.; Chakaravarthy, R.; Ren, W.; Saurina, J.; Suñol, J.J. Structural, Magnetocaloric, and Magnetic Properties in Heusler $Ni_{50}Mn_{35}In_{10}X_5$ (X = Ga, Fe and Al) Alloys. *Metals* **2023**, *13*, 1913. [CrossRef]
3. Elphick, K.; Frost, W.; Samiepour, M.; Kubota, T.; Takanashi, K.; Sukegawa, H.; Miani, S.; Hirohata, A. Heusler alloys for spintronic devices: Review on recent development and future perspectives. *Sci. Technol. Adv. Mater.* **2021**, *22*, 235–271. [CrossRef] [PubMed]

4. Dzekan, D.; Waske, A.; Nielsch, K.; Fähler, S. Efficient and affordable thermomagnetic materials for harvesting low grade waste heat. *APL Mater.* **2021**, *9*, 011105. [CrossRef]
5. Natera, M.G.; Murthy, R.L.; Begum, R.J.; Satya Murthy, N.S. Atomic and magnetic structure of the heusler alloys Pd_2MnGe, Pd_2MnSn, Cu_2MnIn, and CoMnSb. *Phys. Stat. Solidi (a)* **1970**, *3*, 959–964. [CrossRef]
6. Bekhouche, A.; Alleg, S.; Dadda, K.; Daoudi, M.I.; Saurina, J.; Suñol, J.J. Microstructure, martensitic transformation kinetics, and magnetic properties of $(Ni_{50}Mn_{40}In_{10})_{100-x}Co_x$ melt-spun ribbons. *J. Therm. Anal. Calorim.* **2024**, 1–12. [CrossRef]
7. Sun, H.; Jing, C.; Zeng, H.; Su, Y.; Yang, S.; Zhang, Y.; Bachagha, T.; Zhou, T.; Hou, L.; Ren, W. Martensitic Transformation, Magnetic and Mechanical Characteristics in Unidirectional Ni–Mn–Sn Heusler Alloy. *Magnetochemistry* **2022**, *8*, 136. [CrossRef]
8. Dadda, K.; Alleg, S.; Souilah, S.; Suňol, J.J.; Dhahri, E.; Bessais, L.; Hlil, E.K. Critical behavior, magnetic and magnetocaloric properties of melt-spun Ni50Mn35Sn15 ribbons. *J. Alloys Compds.* **2018**, *735*, 1662–1672. [CrossRef]
9. Dhanal, S.V.; Ghaste, A.; Akkimardi, V.G.; Kumar, S. Study of the effect of mechanical alloying on the structure of Ni-Mn-Sn Heusler alloy. *J. Mech. Sci. Technol.* **2020**, *34*, 149–154. [CrossRef]
10. Aksoy, S.; Acet, M.; Deen, P.P.; Mañosa, L.; Planes, A. Magnetic correlations in martensitic Ni-Mn-based Heusler shape-memory alloys: Neutron polarization analysis. *Phys. Rev. B Condens. Matter Mater. Phys.* **2009**, *79*, 212401. [CrossRef]
11. Chabri, T.; Barman, A.; Chatterjee, S.; Mollick, S.A.; Nath, T.K.; Mukherjee, D. Effects of transitional hysteresis on the large magnetocaloric and magnetoresistance properties of Ni-Mn-Co-Sn Heusler alloy. *J Alloys Compds.* **2021**, *863*, 158485. [CrossRef]
12. Ghosh, A.; Mandal, K. Large inverse magnetocaloric effect in $Ni_{48.5-x}Co_xMn_{37}Sn_{14.5}$ (x = 0, 1 and 2) with negligible hysteresis. *J. Alloys Compds.* **2013**, *57*, 9295–9299. [CrossRef]
13. Cong, D.Y.; Roth, S.; Schultz, L. Magnetic properties and structural transformations in Ni–Co–Mn–Sn multifunctional alloys. *Acta Mater.* **2012**, *60*, 5335–5351. [CrossRef]
14. Gao, B.; Hu, F.X.; Shen, J.; Wang, J.; Sun, J.R.; Shen, B.G. Field-induced structural transition and the related magnetic entropy change in $Ni_{43}Mn_{43}Co_3Sn_{11}$ alloy. *J. Magn. Magn. Mater.* **2009**, *321*, 2571–2574. [CrossRef]
15. Zhang, W.Y.; Skomski, R.; Valloppilly, S.R.; Khatri, Y.; Kashyap, A.; Sellmyer, D.J. Magnetism and structure of Fe- and Co-substituted Mn_2NiSn. *J. Magn. Magn. Mater.* **2021**, *537*, 168157. [CrossRef]
16. Liu, F.S.; Wang, Q.B.; Li, S.P.; Ao, W.Q.; Li, J.Q. Effect of Co substitution on the martensitic transformation and magnetocaloric properties of $Ni_{50}Mn_{35-x}Co_xSn_{15}$. *Powd. Diff.* **2013**, *28*, S22–S27. [CrossRef]
17. Yang, L.H.; Zhang, H.; Hu, F.X.; Sun, J.R.; Pan, L.Q.; Shen, B.G. Magnetocaloric effect and martensitic transition in $Ni_{50}Mn_{36-x}Co_xSn_{14}$. *J. Alloys Compds.* **2014**, *588*, 46–48. [CrossRef]
18. Wang, W.; Yu, J.; Zhai, Q.; Luo, Z.; Zheng, H. Co-doping effect on the martensitic transformation and magnetic properties of $Ni_{49}Mn_{39}Sn_{12}$ alloy. *J. Magn. Magn. Mater.* **2013**, *346*, 103–106. [CrossRef]
19. Lutterotti, L. MAUD. 2023. Available online: https://github.com/luttero/Maud (accessed on 6 July 2021).
20. Chen, F.; Tong, Y.X.; Huang, Y.J.; Tian, B.; Li, L.; Zheng, Y.F. Suppression of γ phase in $Ni_{38}Co_{12}Mn_{41}Sn_9$ alloy by melt spinning and its effect on martensitic transformation and magnetic properties. *Intermetallics* **2013**, *36*, 81–85. [CrossRef]
21. de Brito, M.R.; de Souza Silva, F.; Correa, M.A.; Bohn, F.; da Silva, R.B.; dos Passos, T.A.; Torquato, R.A.; Gomes, R.M.; de Oliveira, D.F. Disclosing the role of solidification dynamics on the structural features, magnetic properties and dynamic magnetic behavior of a NiMnSn Heusler alloy. *MRS Commun.* **2022**, *12*, 62–67. [CrossRef]
22. Pérez-Sierra, A.M.; Pons, J.; Santamarta, R.; Vermaut, P.; Ochin, P. Solidification process and effect of thermal treatments on Ni–Co–Mn–Sn metamagnetic shape memory alloys. *Acta Mater.* **2015**, *93*, 164–174. [CrossRef]
23. Czaja, P.; Wierzbicka-Miernik, A. Segregation and microstructure evolution in chill cast and directionally solidified Ni-Mn-Sn metamagnetic shape memory alloys. *J. Cryst. Growth* **2018**, *492*, 50–59. [CrossRef]
24. Schlagel, D.L.; McCallum, R.W.; Lograsso, T.A. Influence of solidification microstructure on the magnetic properties of Ni-Mn-Sn Heusler alloys. *J. Alloys Compd.* **2008**, *463*, 38–46. [CrossRef]
25. Wederni, A.; Ipatov, M.; Pineda, E.; Escoda, L.; González, J.M.; Khitouni, M.; Suñol, J.J. Martensitic transformation, thermal analysis and magnetocaloric properties of Ni-Mn-Sn-Pd alloys. *Processes* **2020**, *8*, 1582. [CrossRef]
26. Mishra, S.S.; Mukhopadhyay, S.; Yadav, T.P.; Yadav, R.M.; Radhakrishnan, S.; Vajtai, R.; Ajayan, P.M.; Mukhopadhyay, N.K.; Singh, H.K.; Srivastava, O.N. Effect of Fe substitution by Co on off-stoichiometric Ni–Fe–Co–Mn–Sn Heusler alloy ribbons. *Mater. Res. Express* **2017**, *4*, 086507. [CrossRef]
27. Kök, M.; Aydoğdu, K.; Kanca, M.S.; Qader, I.N.; Öner, E.; Coşkun, M. Effects of Aging on Magnetic and Thermal Characteristics of NiMnCoSn Magnetic Shape Memory Alloys. *Iran. J. Sci. Technol. Trans. A Sci.* **2021**, *45*, 2191–2199. [CrossRef]
28. Gao, B.; Shen, J.; Hu, F.X.; Wang, J.; Sun, J.R.; Shen, B.G. Magnetic properties and magnetic entropy change in Heusler alloys $Ni_{50}Mn_{35-x}Cu_xSn_{15}$. *Appl. Phys. A* **2009**, *97*, 443–447. [CrossRef]
29. Brown, P.J.; Gandy, A.P.; Ishida, K.; Kainuma, R.; Kanomata, T.; Neumann, K.-U.; Oikawa, K.; Ouladdiaf, B.; Ziebeck, K.R. The magnetic and structural properties of the magnetic shape memory compound $Ni_2Mn_{1.44}Sn_{0.56}$. *J. Phys. Condens. Matter.* **2006**, *18*, 2249–2259. [CrossRef]
30. Chatterjee, S.; Giri, S.; De, S.K.; Majumdar, S. Reentrant-spin-glass state in $Ni_2Mn_{1.36}Sn_{0.64}$ shape-memory alloy. *Phys. Rev. B Condens. Matter Mater. Phys.* **2009**, *79*, 92410. [CrossRef]
31. Jing, C.; Li, Z.; Zhang, H.L.; Chen, J.P.; Qiao, Y.F.; Cao, S.X.; Zhang, J.C. Martensitic transition and inverse magnetocaloric effect in Co doping Ni–Mn–Sn Heusler alloy. *Eur. Phys. J. B* **2009**, *67*, 193–196. [CrossRef]

32. Yan, J.L.; Li, Z.Z.; Chen, X.; Zhou, K.W.; Shen, S.X.; Zhou, H.B. Martensitic transition and magnetocaloric properties in $Ni_{45}Mn_{44-x}Fe_xSn_{11}$ alloys. *J. Alloys Compds.* **2010**, *506*, 516–519. [CrossRef]
33. de Souza Silva, F.; Correa, M.A.; Bohn, F.; Silva, R.B.; Passos, T.A.; Torquato, R.A.; de Lima, B.A.G.; Cordeiro, C.H.N.; Oliveira, D.F. Effect of Nb doping on NiMnSn Heusler alloys: Mechanical, structural, and magnetic properties modifications. *J. Mater. Res. Technol.* **2023**, *26*, 5167–5176. [CrossRef]
34. Dong, S.Y.; Chen, J.Y.; Han, Z.D.; Fang, Y.; Zhang, L.; Zhang, C.L.; Qian, B.; Jiang, X.F. Intermartensitic Transformation and Enhanced Exchange Bias in Pd (Pt)—doped Ni-Mn-Sn alloys. *Sci. Rep.* **2016**, *6*, 25911. [CrossRef]
35. Benali, A.; Bejar, M.; Dhahri, E.; Hlil, E.K.; Graca, M.P.F.; Valente, M.A.; Costa, B.F.O. Assessment of the critical behavior in the multiferroic $Bi_{0.8}Ba_{0.1}Er_{0.1}Fe_{0.96}Cr_{0.02}Co_{0.02}O_3$ material, multi-substitution effect on magnetic and Mössbauer properties. *J. Magn. Magn. Mater.* **2021**, *524*, 167640. [CrossRef]